

Anion Extraction-Induced Polymorph Control of Transition Metal Dichalcogenides

Dae-Hyun Nam,^{†,§} Ji-Yong Kim,^{†,§} Sungwoo Kang,^{†,§} Wonhyo Joo,[†] Seung-Yong Lee,[†] Hongmin Seo,[†] Hyoung Gyun Kim,[†] In-Kyoung Ahn,[†] Gi-Baek Lee,[†] Minjeong Choi,[†] Eunsoo Cho,[†] Miyoung Kim,^{†,‡} Ki Tae Nam,^{†,‡} Seungwu Han,^{†,‡} and Young-Chang Joo^{*,†,‡,§}

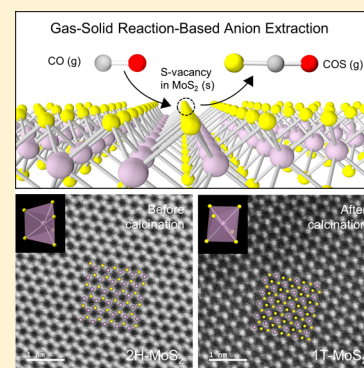
[†]Department of Materials Science and Engineering, Seoul National University, 1 Gwanak-ro, Gwanak-gu, Seoul 08826, Republic of Korea

[‡]Research Institute of Advanced Materials (RIAM), Seoul National University, 1 Gwanak-ro, Gwanak-gu, Seoul 08826, Republic of Korea

Supporting Information

ABSTRACT: Controlled phase conversion in polymorphic transition metal dichalcogenides (TMDs) provides a new synthetic route for realizing tunable nanomaterials. Most conversion methods from the stable 2H to metastable 1T phase are limited to kinetically slow cation insertion into atomically thin layered TMDs for charge transfer from intercalated ions. Here, we report that anion extraction by the selective reaction between carbon monoxide (CO) and chalcogen atoms enables predictive and scalable TMD polymorph control. Sulfur vacancy, induced by anion extraction, is a key factor in molybdenum disulfide (MoS₂) polymorph conversion without cation insertion. Thermodynamic MoS₂–CO–CO₂ ternary phase diagram offers a processing window for efficient sulfur vacancy formation with precisely controlled MoS₂ structures from single layer to multilayer. To utilize our efficient phase conversion, we synthesize vertically stacked 1T-MoS₂ layers in carbon nanofibers, which exhibit highly efficient hydrogen evolution reaction catalytic activity. Anion extraction induces the polymorph conversion of tungsten disulfide (WS₂) from 2H to 1T. This reveals that our method can be utilized as a general polymorph control platform. The versatility of the gas–solid reaction-based polymorph control will enable the engineering of metastable phases in 2D TMDs for further applications.

KEYWORDS: transition metal dichalcogenides, polymorph control, anion extraction, predictive synthesis, hydrogen evolution reaction



Two dimensional transition metal dichalcogenides (TMDs) have attracted significant attention due to their wide range of tunable physical and chemical properties by controlling phase and structure.¹ TMDs exhibit polymorphisms such as trigonal prismatic (1H, 2H) or octahedral (1T) coordination.^{2,3} Polymorph control has enabled the discovery of new intrinsic properties of TMDs such as high electrical conductivity, an active basal plane, increased interlayer spacing, and hydrophilicity.^{4–6} These have induced intriguing efforts to apply molybdenum disulfide (MoS₂) in transistors,⁷ electrocatalysts,^{8,9} supercapacitors,⁴ Li- and Na-ion batteries,¹⁰ actuators,¹¹ superconductors,¹² memristors,¹³ and rectenna for wireless energy harvesting.¹⁴

On the basis of crystal field theory, a polymorph is determined by the electron occupied d-orbital energy level in the transition metal. For the transition from the stable 2H-MoS₂ to the metastable 1T-MoS₂, electron configuration-based strategies, including cation insertion for charge transfer,^{15–20} laser irradiation,⁷ and hot electron injection,²¹ have been explored. However, wet-chemistry-based cation insertion into atomically thin layered TMDs suffers from the limitations of low efficiency, poor controllability, impurity problems, and lab-

scale processes. For example, Li⁺ intercalation requires soaking MoS₂ in *n*-butyllithium solution in an inert atmosphere and takes an extremely long time due to the slow kinetics (Table S1).^{4,5,16,17,22–24} To obtain purified 1T-MoS₂, an additional process is required to remove the inserted cations.¹⁹ Electrochemical Li⁺ intercalation, which proceeds in the battery configuration, received great attention because of its fast and controllable polymorph conversion from 2H- to 1T-MoS₂ by the applied potential.^{18,25} Irradiation-based fabrication is focused on converting a local area of MoS₂ film.⁶ For the frequent situations where the mass production of precisely controlled 1T-MoS₂ is required, the development of a large-scale and systematic method for efficient TMD polymorph control still remains a big challenge.

Here, we report a new fabrication strategy for efficient MoS₂ polymorph control using anion extraction. Instead of inserting cations into a MoS₂ crystal, we extract anions from the MoS₂. The key factor for the polymorph transition without cation

Received: August 8, 2019

Revised: October 8, 2019

Published: October 31, 2019

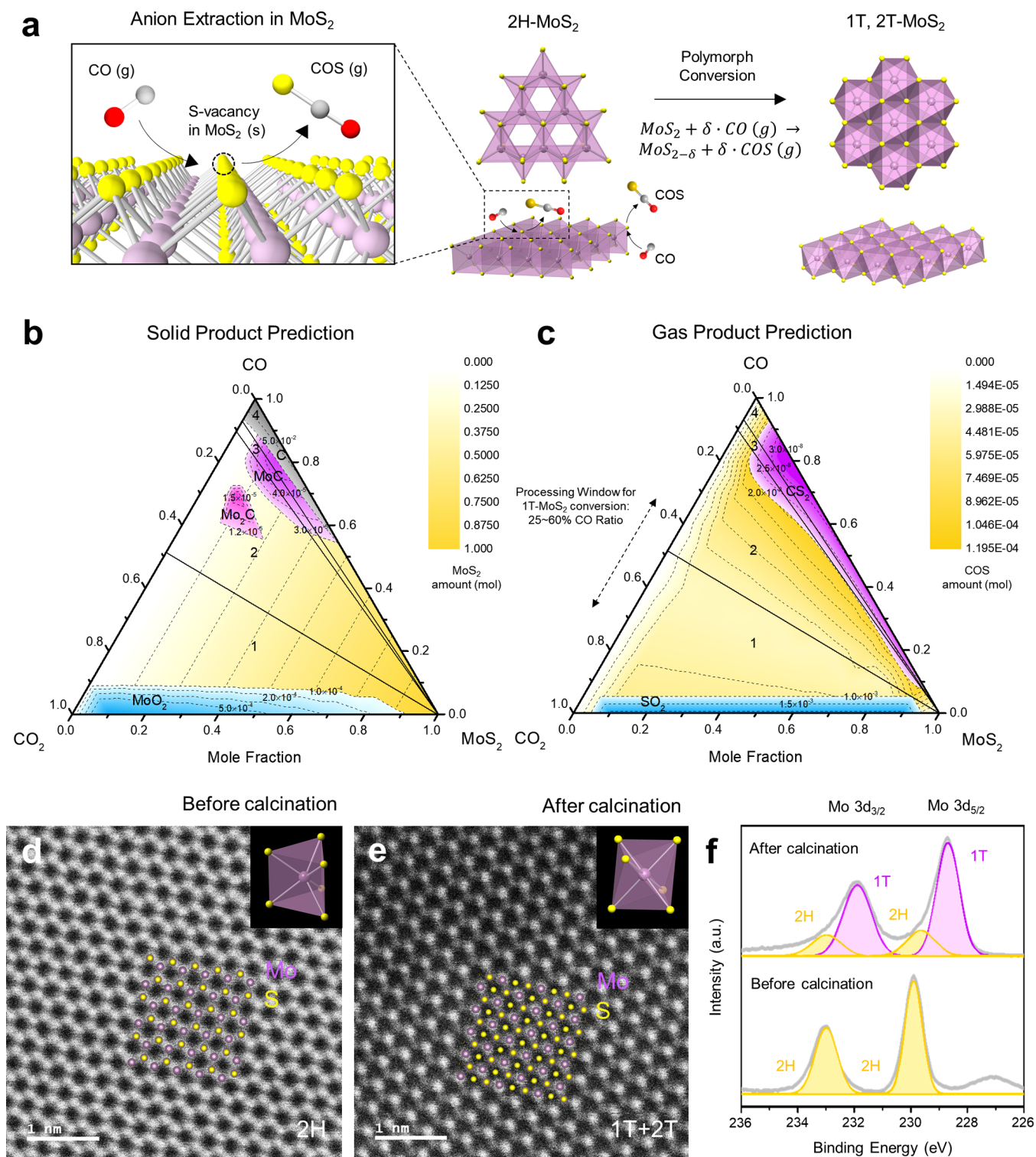


Figure 1. Processing window prediction for anion extraction-based MoS₂ polymorph conversion. (a) CO/CO₂ calcination-based MoS₂ polymorph control by selective reaction between MoS₂ and CO to form V_S. Calculated ternary phase diagrams with (b) solid and (c) gas product distributions at 800 °C calcination to predict MoS₂, CO, and CO₂ mole fractions for 1T-MoS₂ formation. HAADF-STEM images that compare the atomic arrays in MoS₂ flakes for (d) 2H-MoS₂ (before calcination) and (e) 1T+2T-MoS₂ (after calcination). (f) Mo 3d XPS analysis for investigating the conversion from 2H to 1T-MoS₂ by comparing before and after CO/CO₂ calcination (40% CO, 800 °C, and 5 h condition) of MoS₂ powders.

insertion is the sulfur vacancy (V_S) formation. V_S-induced polymorph conversion from 2H to 1T has been suggested by theoretical calculations and experiments.^{26–29} In situ transmission electron microscopy (TEM) study revealed that the formation of α -phase, local strain, and atomic gliding can

induce the 1T-MoS₂ formation.³⁰ The α -phase formation by V_S, local strain, and the 1T-/2H-MoS₂ interface with defects were studied by several experimental works.^{5,27,31,32} In this work, we developed a new gas–solid reaction-based V_S

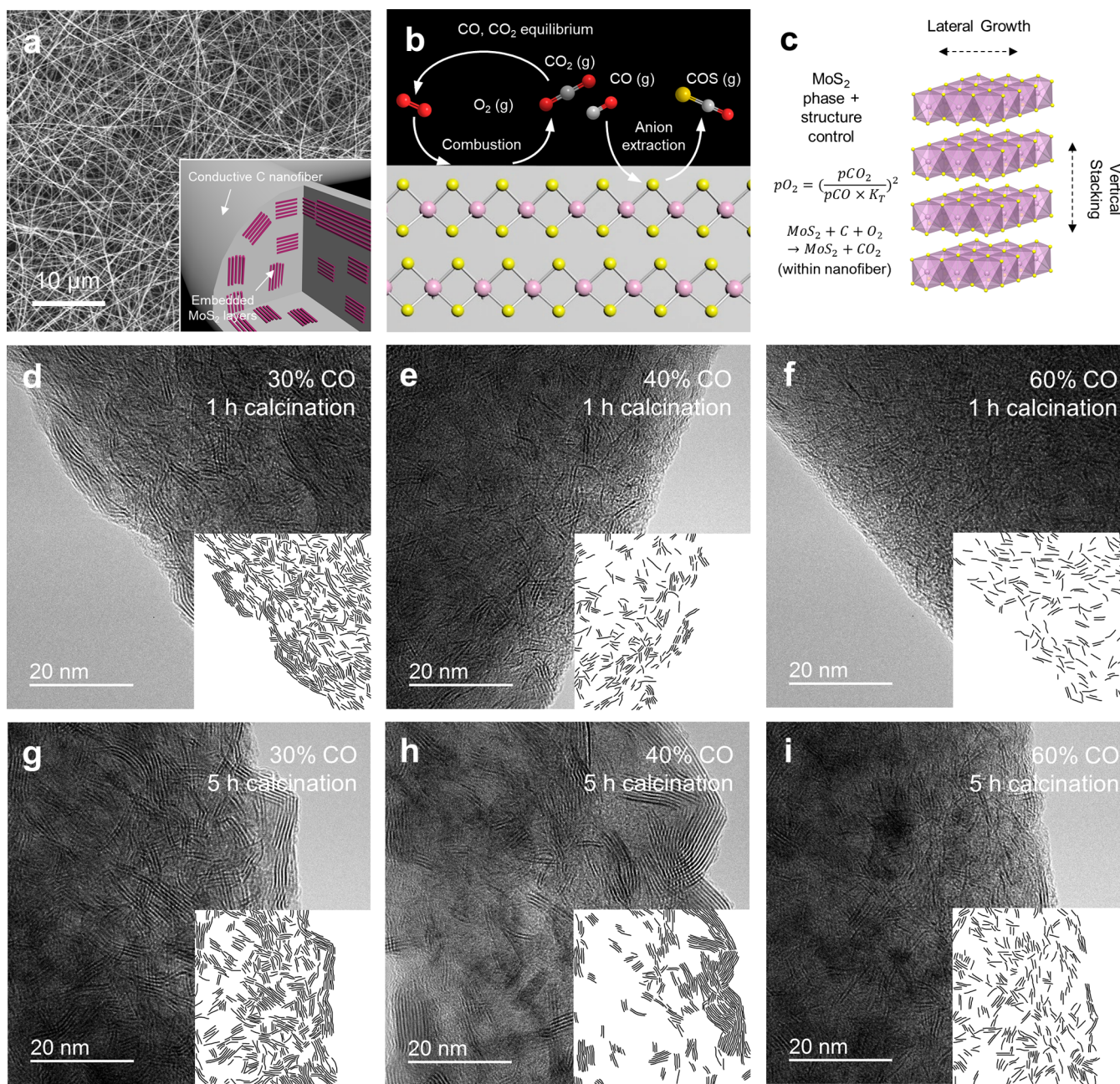


Figure 2. 1T-MoS₂ phase and structure control in MoS₂/CNFs. (a) FE-SEM image of ATTM+PAN nanofibers that transform into MoS₂/CNFs (schematic) via CO/CO₂ calcination. (b) Schematic of gas–solid reaction between CO, CO₂, and MoS₂/CNFs to induce selective C oxidation and anion extraction. (c) MoS₂ stacking number and layer length control scheme with phase control. (d–i) TEM images of MoS₂/CNFs according to the CO ratio and isothermal time of calcination. Black lines in inlet display the distribution of self-assembled MoS₂ layers within CNFs.

formation methodology which can realize the tunable polymorph control in large scale material fabrication.

Inspired by chemical metallurgy, in which oxygen is extracted from a metal ore (Fe₂O₃) for metal (Fe) reduction, calcination under a carbon monoxide (CO)/carbon dioxide (CO₂) mixed gas was applied in our methodology.³³ In this system, various compounds can be formed by the redox reaction between molybdenum (Mo), sulfur (S), carbon (C), and oxygen (O) elements. To drive a selective reaction between CO and S while preventing others, we designed a processing map for the specific reaction pathway. In particular, the processing window to generate V_S along with carbonyl sulfide (COS) was predicted by calculating MoS₂–CO–CO₂

ternary phase diagram using thermodynamic chemical potential of each compound. The 2H to 1T phase ratio was controlled by the predicted processing parameters. This can modulate the MoS₂ polymorph, regardless of the material form factor (flake, film, or precursor) and even when the MoS₂ layer is incorporated into a C matrix. Simultaneous MoS₂ structure (vertical stacking, lateral growth) and polymorph (2H, 1T) control was realized by self-assembled 1T-MoS₂ layers in carbon nanofibers (CNFs). Our predictive approach enables the efficient and rapid synthesis of 1T-MoS₂ by applying a specific molar composition of MoS₂–CO–CO₂ for the targeted reaction. This work paves the way to optimize the

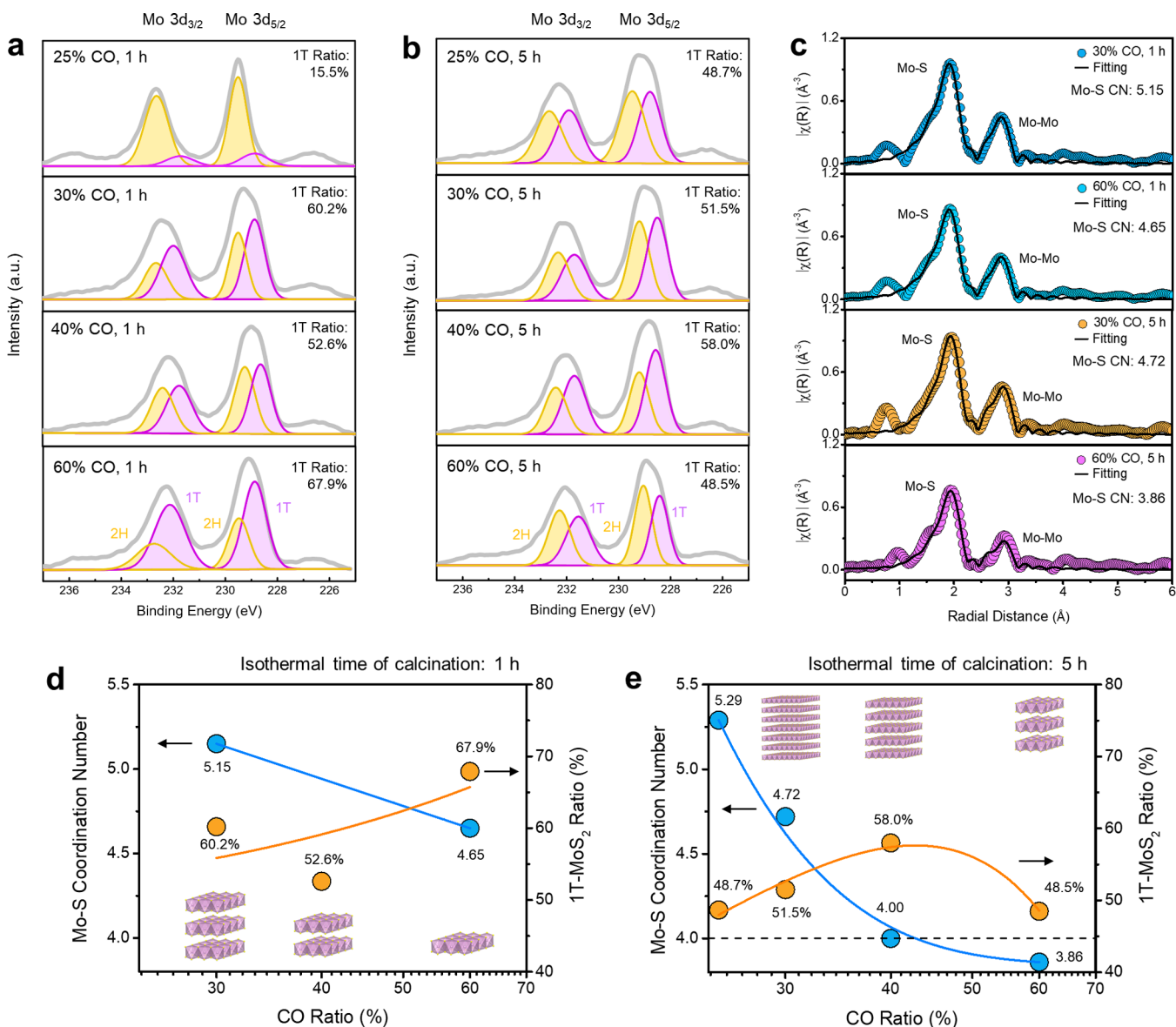
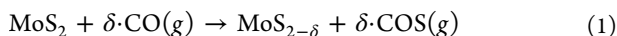


Figure 3. Anion extraction induced 1T-MoS₂ polymorph control kinetics. XPS analysis of Mo 3d for the investigation of the relative ratio between the 1T and 2H phases of MoS₂/CNFs according to the CO ratio at calcination isothermal times of (a) 1 h and (b) 5 h at 800 °C. (c) EXAFS spectra with fitting for investigating the local atomic structures (coordination number, atomic distance) of Mo–S in MoS₂/CNFs according to the CO ratio (30 and 60%) after 1 and 5 h of calcination. The relationship between Mo–S coordination number, MoS₂ structure (stacking number and length), and 1T-MoS₂ ratio of MoS₂/CNFs were investigated according to the CO ratio for (d) 1 h and (e) 5 h CO/CO₂ calcination.

intrinsic properties of metastable TMDs by the kinetically fast anion extraction approach.

Through introduction of CO into MoS₂, the S atoms coordinated around the Mo atom react with CO to generate COS along with V_S (Figure 1a). This V_S formation with CO adsorption can induce octahedral 1T-MoS₂.



eq 1 displays the process of nonstoichiometric/defective 1T-MoS₂ formation by anion extraction.

The processing window for V_S formation by anion extraction was predicted by calculating MoS₂–CO–CO₂ ternary phase diagrams.^{34,35} To determine the CO:CO₂ ratio and the mole fraction of MoS₂, we calculated the solid and gas product distributions at the calcination condition of 800 °C and 1 atm (Figure 1b, c). In the diagram, region 1 displays MoS₂ (s) + MoO₂ (s) + gas; region 2 displays MoS₂ (s) + Mo₂C (s) + gas;

region 3 displays MoS₂ (s) + MoC (s) + gas; and region 4 displays MoS₂ (s) + MoC (s) + C (s) + gas. We constructed a contour map of the product distribution according to the mole fraction of MoS₂–CO–CO₂ (starting materials) and overlapped it with the ternary phase diagram (Figure S3, Table S2, S3). The solid lines are tie lines that indicate stable intermediate compound formation, and the dashed lines show the changes in the calculated product amounts according to the specific composition of the starting materials.³⁶

In the solid product prediction map (Figure 1b), MoS₂, molybdenum oxide (MoO₂), molybdenum carbide (Mo₂C, MoC), and C were calculated to be the main products. In the MoS₂ distribution (yellow), the MoS₂ amount after reaction was mainly affected by the initial MoS₂ mole fraction. As the CO mole fraction decreased to lower than 0.125, MoO₂ (blue) started to be generated. This is due to the increased oxygen partial pressure (pO₂) over that of the formation Gibbs free

energy (ΔG°_f) for MoO_2 .³⁴ In the MoS_2 thermal treatment, preventing MoO_2 formation is essential because MoO_2 has a ΔG°_f lower than that of MoS_2 (ΔG°_f of $\text{MoO}_2 = -395.59$ kJ/mol and ΔG°_f of $\text{MoS}_2 = -201.22$ kJ/mol at 800 °C).³⁴ In this regard, p_{O_2} should be lower than that of the ΔG°_f for MoO_2 to prevent MoS_2 oxidation to MoO_2 . When the CO mole fraction increased to over 0.7, Mo_2C (pink) and MoC (purple) were expected to be formed. At a higher CO mole fraction of over 0.9, C (gray) was expected to be precipitated based on the Boudouard reaction of $\text{C}(\text{s}) + \text{CO}_2(\text{g}) \leftrightarrow 2\text{CO}(\text{g})$. A CO ratio from 20 to 70% was determined to be a safe zone for the homogeneous MoS_2 without phase overlap at any MoS_2 mole fraction.

In the gas product prediction map (Figure 1c), COS, sulfur dioxide (SO_2), and carbon disulfide (CS_2) were determined to be the main gas products. At the low CO ratio range, SO_2 was generated due to the MoO_2 formation. At the high CO ratio range, CS_2 was generated, and it was related with the C precipitation and Mo_2C and MoC formation. Tracking the COS (yellow) amount according to the CO ratio is important because the COS directly indicates the V_S formation in the MoS_2 . Interestingly, we found a valley region where the calculated amount of COS increases gradually with the CO ratio. We expected that an experiment in this region could induce the anion extraction-based MoS_2 polymorph conversion. Therefore, considering the solid and gas product prediction maps, we set the CO ratio from 25 to 60% as a processing window for 1T- MoS_2 conversion.

On the basis of this predicted condition, we calcined MoS_2 powder under CO/ CO_2 gas (40% CO ratio) at 800 °C for 5 h. The atomic arrangement of MoS_2 on the c -axis plane was investigated by Cs-corrected TEM to compare the MoS_2 status before and after calcination. High-angle annular dark-field imaging scanning TEM (HAADF-STEM) contrast displays heavy atoms (Mo) with higher intensity (bright) than light atoms (S). Purple and yellow inlet dots on HAADF-STEM images indicate Mo and S atoms (Figure 1d and 1e). The HAADF-STEM image of the MoS_2 layers before calcination indicates a 2H- MoS_2 atomic array (Figure 1d). After calcination, the atomic array was transformed to the T phase according to HAADF-STEM (Figure 1e) along the [0001] direction.³⁷ In Figure 1e, the brightness of the Mo atoms varies according to the Mo position, and this can be observed when 1T- and 2T- MoS_2 coexist in the MoS_2 multilayer (Figure S6). In this work, the 1T phase represents the entire T phase, including 1T- and 2T- MoS_2 .³⁷ We compared the status of MoS_2 powders from before and after calcination by Raman and Mo 3d X-ray photoelectron spectroscopy (XPS) analyses. In Raman analysis (Figure S9), we confirmed the clear peaks of J_1 , J_2 , and J_3 after the calcination, which indicate the existence of the 1T phase.³⁸ By deconvoluting the XPS spectra of Mo 3d_{3/2} and Mo 3d_{5/2}, we verified the formation of high purity 1T- MoS_2 (Figure 1f). Also, the XPS S 2p spectra shift to lower binding energy supports the conversion from 2H- to 1T- MoS_2 (Figure S10).^{19,23}

To extend the applicable material range of the anion extraction approach, the MoS_2 polymorph transition was applied in MoS_2 /CNFs (Figure 2a). We fabricated MoS_2 /CNFs by calcining electrospun ammonium tetrathiomolybdate (ATTM, $(\text{NH}_4)_2\text{MoS}_4$) + polyacrylonitrile (PAN, $\text{C}_3\text{H}_3\text{N}$) nanofibers. When the MoS_2 nanocrystals were incorporated into the CNFs, the stacking number and layer length of the MoS_2 layers could be controlled with polymorph conversion.

In MoS_2 /CNFs, anion extraction-based polymorph conversion needs to proceed in the specific thermodynamic region where selective C oxidation and Mo sulfidation are induced with preventing other reactions in the Mo-S-C-O quaternary system (Figure 2b).³⁴ Simultaneous MoS_2 phase and structure control can be realized because gaseous CO can penetrate the C matrix for the reaction with MoS_2 (Figure 2c).

In the TEM images of MoS_2 /CNFs, we observed that the 1T- MoS_2 structures are controlled from single- to multilayers according to the CO ratio and isothermal time of calcination (Figure 2d-i). As the CO ratio decreased from 60 to 30% (increasing p_{O_2}), the vertical stacking and lateral growth of the MoS_2 layers were promoted. As the isothermal time increased from 1 to 5 h, the MoS_2 stacking number and layer length increased accordingly. This phenomenon occurs because the CO reacts with the S in MoS_2 , and the O_2 , controlled by the equilibrium reaction between CO and CO_2 , reacts with C, as displayed in Figure 2b. As p_{O_2} increases with the decreasing CO ratio, the degree of C combustion increases.³⁴ This promotes the nucleation and growth of MoS_2 nanocrystals in CNFs.

We analyzed the Mo 3d XPS spectra according to the CO ratio (25, 30, 40, and 60%) and the isothermal time (1 and 5 h) of CO/ CO_2 calcination to quantify the degree of polymorph conversion in MoS_2 /CNFs (Figure 3a and 3b). The 1T- MoS_2 ratio in the MoS_2 /CNFs increased as the CO ratio and isothermal time increased. At the lowest CO ratio of 25%, the MoS_2 was almost all in the 2H phase after 1 h of calcination. As the CO ratio increased from 25 to 60%, the 1T- MoS_2 proportion increased from 15.5 to 67.9%. After 5 h of calcination, the 1T- MoS_2 proportion gradually increased from 48.7 to 58.0% as the CO ratio increased from 25 to 40%. However, at the critical point of the highest CO ratio and isothermal time (60% CO and 5 h), the degree of polymorph transition degraded to 48.5% (Figure S14).

To verify that the 1T- MoS_2 conversion is related to V_S , we carried out Mo K-edge X-ray absorption spectroscopy (XAS) analysis according to processing parameters. Extended X-ray absorption fine structure (EXAFS) spectra display the V_S generation tendency in MoS_2 /CNFs according to the CO ratio after 1 and 5 h of calcination (Figure 3c). EXAFS fitting provided the information on the S atom coordination number (CN) around the Mo atom (Table S4). Normally, the Mo atom in MoS_2 is coordinated with six S atoms. In the MoS_2 /CNFs after 5 h of calcination, the Mo-S CN of MoS_2 at the 25% CO ratio condition was 5.29 ± 0.44 . As the CO ratio increased to 30%, the Mo-S CN decreased to 4.72 ± 0.36 . At 40 and 60% CO, the Mo-S CNs decreased to 4.00 ± 0.27 and 3.86 ± 0.39 , respectively (Figure 3c, Figure S17). Also, in the 1 h calcination of MoS_2 /CNFs, Mo-S CN decreased from 5.15 ± 0.44 to 4.65 ± 0.40 when the CO ratio increase from 30 to 60%.

While the Mo-S CN was controlled according to the CO ratio, XRD revealed that the MoS_2 phase was maintained at this processing window (Figure S19). We evaluated the precision of processing window by proceeding with the calcination at the 20% CO ratio, lower CO condition than the boundary for homogeneous MoS_2 formation. Interestingly, we found that the calcination of ATTM + PAN nanofibers forms the mixed phase of MoS_2 and MoO_2 , predicted in MoS_2 -CO- CO_2 ternary phase diagram (Figure S20). This reveals that our method provides a precise information for the synthesis in terms of polymorph and overall phase of materials.

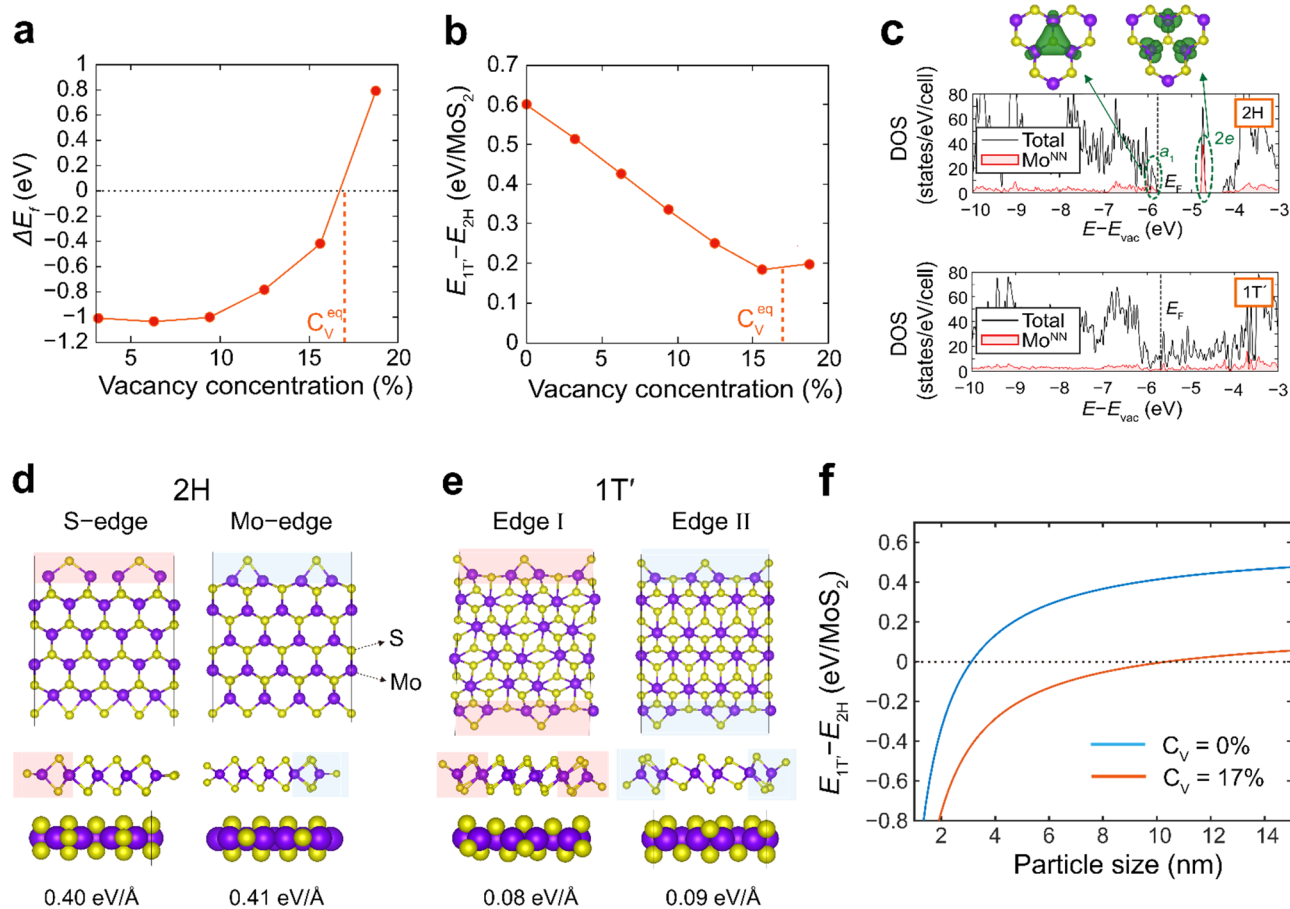


Figure 4. First-principles study of MoS₂ polymorph transition by CO. (a) ΔE_f of monolayer 1T'-MoS₂ as a function of the vacancy concentration. (b) $E_{1T'} - E_{2H}$ per unit MoS₂ as a function of the V_S concentration. (c) DOS of monolayer 2H-MoS₂ and 1T'-MoS₂ with 3.125% V_S , which are aligned by the vacuum level (E_{vac}). Morphologies and edge energies of monolayer (d) 2H- and (e) 1T'-MoS₂. (f) $E_{1T'} - E_{2H}$ as a function of the particle size for pure MoS₂ and V_S -induced MoS₂. The effects of the vacancies and nanoparticle size were calculated analytically using $E_{1T'} - E_{2H}$ and MoS₂ edge energy data.

Gas products during the CO/CO₂ calcination of MoS₂/CNFs were investigated for the experimental verification of the anion extraction by CO (Figure S21). As we predicted in thermodynamic calculation (Figure 1c), COS, SO₂, and CS₂ were detected, and their amount was changed according to the CO ratio. Especially, the amount of COS increased as the CO ratio increased. This result reveals the reaction between CO and S and the V_S formation in the MoS₂. With the EXAFS and gas detection results, it has been verified that the V_S of MoS₂ increases when CO ratio increases.

To find out the effect of V_S and the MoS₂ structure in the anion extraction-based polymorph conversion, the distributions of the Mo-S CN, MoS₂ structure, and 1T-MoS₂ ratio in the MoS₂/CNFs were merged according to the processing parameters (Figure 3d and 3e). The decrease of the Mo-S CN from the EXAFS spectra can be interpreted as the number of V_S increases in the MoS₂. We discovered a strong relationship between V_S and the 1T-MoS₂ formation. After 1 and 5 h of calcination, the 1T-MoS₂ ratio increased as the number of V_S increased according to the CO ratio. In the 5 h calcination of MoS₂/CNFs, which induced lower Mo-S CN than that of 1 h calcination, 1T-MoS₂ ratio increased from 48.66 to 57.99% as the Mo-S CN decreased from 5.29 ± 0.44 to 4.00 ± 0.27 . However, when the Mo-S CN decreased to below 4, the 1T-MoS₂ ratio decreased (57.99% at 4.00 ± 0.27 Mo-S CN \rightarrow 48.48% at 3.86 ± 0.39 Mo-S CN). This might be related to

the phase instability of MoS₂ at high V_S concentration (C_V), and Mo-S CN of 4 is expected as a limiting point for the efficient 1T-MoS₂ conversion by anion extraction.

As the isothermal time increased from 1 to 5 h, the vertical stacking and lateral growth of the MoS₂ intensified. When we compared the 1T-MoS₂ ratios according to the isothermal time at the same CO ratio, the 1T-MoS₂ ratio in the MoS₂/CNFs and the Mo-S CN decreased as the isothermal time increased. This phenomenon is related to the effect of the MoS₂ morphology on the polymorph transition. As the MoS₂ size increases, the degree of polymorph conversion decreases. We confirmed that the V_S from anion extraction can induce 1T-MoS₂ conversion with a reaction rate that is affected by the MoS₂ structure.

We performed density functional theory (DFT) calculations to investigate theoretically the role of V_S on the TMD polymorph conversion and compared the relative stabilities of the 1T' and 2H phases under various conditions (1T' is known to be more stable than 1T.^{39–41}). To estimate the equilibrium V_S concentration (C_V^{eq}), we investigated the differential vacancy formation energy (ΔE_f) of 1T'-MoS₂ as a function of C_V , assuming a uniform distribution of vacancies. ΔE_f is defined by the following equation:

$$\Delta E_f = \mu_S + E^{n+1} - E^n \quad (2)$$

where n is the number of vacancies in the 4×4 supercell, E^n is the DFT energy of the supercell, and μ_S is the chemical potential of S. μ_S is determined by the equilibrium condition between CO and COS:

$$\mu_S = E_{\text{COS}} - E_{\text{CO}} + \Delta E_{\text{ZPE}} - T\Delta S + kT \ln(p_{\text{COS}}/p_{\text{CO}}) \quad (3)$$

where E_{COS} and E_{CO} are the DFT energies of COS and CO, ΔE_{ZPE} is the zero-point energy difference, ΔS is the entropy difference taken from the NIST database,⁴² p_{COS} and p_{CO} are the partial pressures of COS (10 ppm, 10^{-5} atm) and CO (0.5 atm) inferred from the experiment, and the temperature (T) is set to the experimental value of 1073 K.

Figure 4a shows ΔE_f as a function of C_V . ΔE_f is constant (~ -1.0 eV) at the isolated limit ($C_V \leq 9\%$) and increases with C_V , becoming positive from above $C_V = 19\%$. The C_V^{eq} was calculated as 17%, which was set to be the minimum point of Gibbs free energy (G) including the configurational entropy of V_S in eq 2. This value elucidates the feasibility of V_S formation by the reaction between CO and MoS₂. Figure 4b shows the energy difference between monolayer 1T' and 2H-MoS₂ ($E_{1T'} - E_{2H}$), which is in good agreement with the previous works on $E_{1T'} - E_{2H}$ in the presence of V_S .^{26,27} The $E_{1T'} - E_{2H}$ decreases significantly from 0.60 eV/MoS₂ (without V_S) to 0.22 eV/MoS₂ (at C_V^{eq}) with increasing C_V . We determined that the equilibrium C_V^{eq} and corresponding $E_{1T'} - E_{2H}$ of multilayer MoS₂ are almost identical to the monolayer values. This indicates that increasing C_V can promote the 1T' phase conversion. Also, the increase of $E_{1T'} - E_{2H}$ by the excessive V_S formation can be related with the decreased 1T-MoS₂ ratio (Figure 3e).

To understand how V_S affects the relative stability of the two phases, we present the partial densities of states (PDOS) for 3.125% V_S in 2H-MoS₂ and 1T'-MoS₂ monolayers (Figure 4c). The PDOS of the V_S -induced 2H-MoS₂ is in good agreement with the previous calculation,⁴³ where one occupied a_1 level and two unoccupied e levels are generated as a result of hybridization among the d orbitals of three Mo atoms near V_S (Mo^{NN}). The a_1 state of 1T'-MoS₂ is located in the valence d -band, and the e states are located in the conduction d -band, similar to the anion vacancy states of group 4 TMDs.^{44–46} Therefore, the electrons in the a_1 state are stabilized in the T' phase, which reduces $E_{1T'} - E_{2H}$ and induces the 1T' phase conversion.

We investigated the effect of MoS₂ structure on the polymorph control. The relative energy difference between 1T' and 2H-MoS₂ varies with the MoS₂ particle size because of the edge-energy difference.⁴⁷ Figure 4d and 4e show two types of edges at 2H-MoS₂ and 1T'-MoS₂, respectively. The termination and energies of edges are calculated by the ribbon model and nanoparticle structure (see Supporting Information for details). The average edge energies were calculated as 0.40 eV/Å for 2H- and 0.09 eV/Å for 1T'-MoS₂. $E_{1T'} - E_{2H}$ as a function of the nanoparticle size was estimated using the average edge energies (Figure 4f). The effect of V_S was considered a constant shift of $E_{1T'} - E_{2H}$, according to the values presented in Figure 4b. Note that vacancy formation at the edge sites was ignored because vacancy formation energy at the edge sites is much larger than that of the basal plane (Table S6). While pure 1T'-MoS₂ is more stable than 2H-MoS₂ in the range of particle sizes below 2 nm, the V_S -induced 1T'-MoS₂ can be stabilized until the particle size is approximately 10 nm. As C_V increases, the size of the MoS₂ flake for stable 1T' phase

increases. This reveals that V_S can stabilize the formation of 1T'-MoS₂ at larger size of MoS₂ particle.

To prove the merit of simultaneous MoS₂ structure and phase control, we evaluated the electrochemical catalytic activity of the 1T-MoS₂/CNFs (Figure S25).³⁴ This anion extraction approach can make 1T-MoS₂, optimize the MoS₂ structure, and hybridize MoS₂ with an electrically conductive C matrix at the same time. Based on this, we fabricated vertically aligned MoS₂ in CNFs with 1T-MoS₂ ratios of 0, 25, and 58%. The hydrogen evolution reaction (HER) activity of the MoS₂/CNFs was measured in a 0.5 M H₂SO₄ electrolyte. Figure 5a

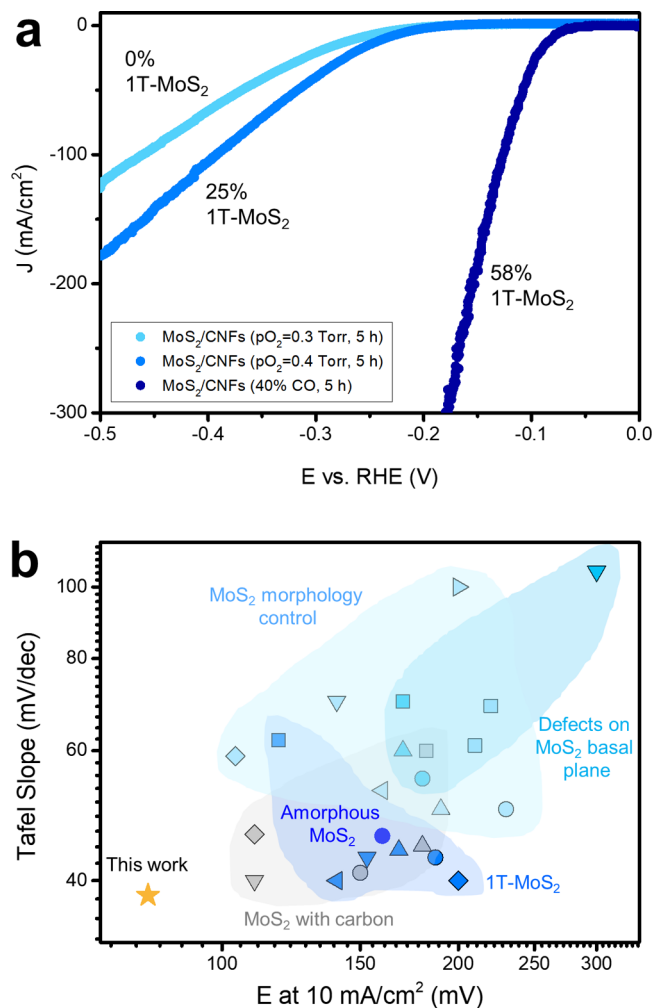


Figure 5. Catalytic activity of polymorph and structure controlled MoS₂/CNFs. (a) Effect of 1T phase on the HER catalytic activity of MoS₂/CNFs with LSV. (b) Comparing the HER performances of MoS₂-based electrocatalysts in terms of the potential at 10 mA/cm² and Tafel slope.^{9,16,52–61,17,62–66,18,19,25,48–51}

shows a comparison of the linear sweep voltammetry (LSV). As the 1T-MoS₂ ratio increased, the HER performance was boosted in terms of the onset potential, overpotential, and Tafel slope. MoS₂/CNFs with 58% 1T phase exhibited 80.5 mV as the lowest potential at 10 mA/cm² with a Tafel slope of 38.2 mV/dec (Figure 5b). Compared to other MoS₂-based HER electrocatalysts, our 1T-MoS₂/CNFs with the optimized MoS₂ phase and structure showed a superior catalytic performance. This can be explained by the promoted H adsorption at the 1T-MoS₂ basal plane (lower activation

barrier in the Volmer step) and the optimized MoS₂ structures within the highly conductive CNFs.⁴⁰

This method was applied to tungsten disulfide (WS₂) polymorph control to extend the application range. We found the processing window for V_S formation in WS₂ by calculating WS₂–CO–CO₂ ternary phase diagrams with solid and gas products (Figure S27). Compared to MoS₂, WS₂ showed the wider region for the W oxide (W₁₈O₄₉, WO₂) formation. Above the CO ratio for W oxide, we found the valley region to form 1T-WS₂, where the COS amount increases with CO ratio. After we calcined the ammonium tetrathiotungstate ((NH₄)₂WS₄) + PAN nanofibers, 1T-WS₂/CNFs were fabricated successfully. This result reveals that the anion extraction can be applied as a general method for polymorph control.

In summary, we developed a new TMD polymorph control platform using an anion extraction approach that mediates the bonding between the gas-phase reactant and the solid target material. Starting from DFT calculations to discover V_S as a key factor leading to the T phase transition, we systematically controlled the MoS₂ polymorph by a gaseous CO reaction with the S atoms adjacent to Mo atoms to form V_S in the MoS₂. The processing window for the experiment was designed according to the MoS₂–CO–CO₂ ternary phase diagram. Based on the processing parameters to generate V_S, the 1T-MoS₂ in the MoS₂/CNFs was precisely controlled. We established a V_S–MoS₂ structure–polymorph relationship wherein the MoS₂ stacking number and layer length affect the V_S-induced 1T-MoS₂ formation. This work can open an avenue for not only the TMD polymorph transition but also predictive nanofabrication via a thermodynamically designed reaction pathway. We envision that the fabrication advantages of gas medium-based anion extraction such as precise controllability, predictive synthesis, and mass production can be extended toward higher-order atomic component systems.

■ ASSOCIATED CONTENT

Supporting Information

The Supporting Information is available free of charge on the ACS Publications website at DOI: 10.1021/acs.nanolett.9b03240.

Materials and methods, theoretical DFT calculation about 1T-MoS₂ conversion, thermodynamic calculation for processing parameter prediction, TEM, Raman, XRD, XAS analysis of 1T-MoS₂/CNFs, gas detection experiment result, effect of CO/CO₂ calcination temperature on polymorph control, Tafel slope of 1T-MoS₂/CNFs and HER activity comparison with others, and polymorph control of WS₂/CNFs (Figures S1–S27, Tables S1–S9) (PDF)

■ AUTHOR INFORMATION

Corresponding Author

*E-mail: ycjoo@snu.ac.kr.

ORCID

Dae-Hyun Nam: 0000-0002-0871-1355

Miyoung Kim: 0000-0001-8632-6711

Ki Tae Nam: 0000-0001-6353-8877

Young-Chang Joo: 0000-0003-2562-375X

Author Contributions

[§]D.-H.N., J.-Y.K., and S.K. contributed equally to this work.

Notes

The authors declare no competing financial interest.

■ ACKNOWLEDGMENTS

This research was supported by Creative Materials Discovery Program through the National Research Foundation of Korea (NRF) funded by the Ministry of Science, ICT and Future Planning (2017M3D1A1040688). The computation was carried out at the KISTI supercomputing center (Grant KSC-2018-C3-0022). Atomic-resolution STEM images were acquired using a JEOL ARM-200CF TEM instrument installed at the National Center for Interuniversity Research Facilities (NCIRF) at Seoul National University. Y.-C.J. thanks Philip Kim (Harvard University) for discussion.

■ REFERENCES

- (1) Zhang, Z.; Chen, P.; Duan, X.; Zang, K.; Luo, J.; Duan, X. *Science* **2017**, *357*, 788–792.
- (2) Chhowalla, M.; Shin, H. S.; Eda, G.; Li, L.-J.; Loh, K. P.; Zhang, H. *Nat. Chem.* **2013**, *5*, 263–275.
- (3) Fan, X.; Xu, P.; Zhou, D.; Sun, Y.; Li, Y. C.; Nguyen, M. A. T.; Terrones, M.; Mallouk, T. E. *Nano Lett.* **2015**, *15*, 5956–5960.
- (4) Acerce, M.; Voiry, D.; Chhowalla, M. *Nat. Nanotechnol.* **2015**, *10*, 313.
- (5) Koppera, R.; Voiry, D.; Yalcin, S. E.; Branch, B.; Gupta, G.; Mohite, A. D.; Chhowalla, M. *Nat. Mater.* **2014**, *13*, 1128.
- (6) Yu, Y.; Nam, G.-H.; He, Q.; Wu, X.-J.; Zhang, K.; Yang, Z.; Chen, J.; Ma, Q.; Zhao, M.; Liu, Z.; et al. *Nat. Chem.* **2018**, *10*, 638–643.
- (7) Cho, S.; Kim, S.; Kim, J. H.; Zhao, J.; Seok, J.; Keum, D. H.; Baik, J.; Choe, D.-H.; Chang, K. J.; Suenaga, K.; et al. *Science* **2015**, *349* (6248), 625–628.
- (8) Voiry, D.; Fullon, R.; Yang, J.; de Carvalho Castro e Silva, C.; Koppera, R.; Bozkurt, I.; Kaplan, D.; Lagos, M. J.; Batson, P. E.; Gupta, G.; et al. *Nat. Mater.* **2016**, *15*, 1003–1009.
- (9) Tan, C.; Luo, Z.; Chaturvedi, A.; Cai, Y.; Du, Y.; Gong, Y.; Huang, Y.; Lai, Z.; Zhang, X.; Zheng, L.; et al. *Adv. Mater.* **2018**, *30*, 1705509.
- (10) Geng, X.; Jiao, Y.; Han, Y.; Mukhopadhyay, A.; Yang, L.; Zhu, H. *Adv. Funct. Mater.* **2017**, *27*, 1702998.
- (11) Acerce, M.; Akdoğan, E. K.; Chhowalla, M. *Nature* **2017**, *549*, 370–373.
- (12) Ye, J. T.; Zhang, Y. J.; Akashi, R.; Bahramy, M. S.; Arita, R.; Iwasa, Y. *Science* **2012**, *338*, 1193–1196.
- (13) Cheng, P.; Sun, K.; Hu, Y. H. *Nano Lett.* **2016**, *16*, 572–576.
- (14) Zhang, X.; Grajal, J.; Vazquez-Roy, J. L.; Radhakrishna, U.; Wang, X.; Chern, W.; Zhou, L.; Lin, Y.; Shen, P.-C.; Ji, X.; et al. *Nature* **2019**, *566* (7744), 368–372.
- (15) Yang, H.; Kim, S. W.; Chhowalla, M.; Lee, Y. H. *Nat. Phys.* **2017**, *13*, 931–937.
- (16) Lukowski, M. A.; Daniel, A. S.; Meng, F.; Forticaux, A.; Li, L.; Jin, S. *J. Am. Chem. Soc.* **2013**, *135*, 10274–10277.
- (17) Voiry, D.; Salehi, M.; Silva, R.; Fujita, T.; Chen, M.; Asefa, T.; Shenoy, V. B.; Eda, G.; Chhowalla, M. *Nano Lett.* **2013**, *13*, 6222–6227.
- (18) Wang, H.; Lu, Z.; Xu, S.; Kong, D.; Cha, J. J.; Zheng, G.; Hsu, P.-C.; Yan, K.; Bradshaw, D.; Prinz, F. B.; et al. *Proc. Natl. Acad. Sci. U. S. A.* **2013**, *110*, 19701–19706.
- (19) Liu, L.; Wu, J.; Wu, L.; Ye, M.; Liu, X.; Wang, Q.; Hou, S.; Lu, P.; Sun, L.; Zheng, J.; et al. *Nat. Mater.* **2018**, *17*, 1108–1114.
- (20) Zhang, J.; Yang, A.; Wu, X.; van de Groep, J.; Tang, P.; Li, S.; Liu, B.; Shi, F.; Wan, J.; Li, Q.; et al. *Nat. Commun.* **2018**, *9*, 5289.
- (21) Kang, Y.; Najmaei, S.; Liu, Z.; Bao, Y.; Wang, Y.; Zhu, X.; Halas, N. J.; Nordlander, P.; Ajayan, P. M.; Lou, J.; et al. *Adv. Mater.* **2014**, *26*, 6467–6471.
- (22) Maitra, U.; Gupta, U.; De, M.; Datta, R.; Govindaraj, A.; Rao, C. N. R. *Angew. Chem.* **2013**, *125*, 13295–13299.

- (23) Liu, Q.; Li, X.; He, Q.; Khalil, A.; Liu, D.; Xiang, T.; Wu, X.; Song, L. *Small* **2015**, *11*, 5556–5564.
- (24) Lei, Z.; Zhan, J.; Tang, L.; Zhang, Y.; Wang, Y. *Adv. Energy Mater.* **2018**, *8*, 1703482.
- (25) Wang, H.; Lu, Z.; Kong, D.; Sun, J.; Hymel, T. M.; Cui, Y. *ACS Nano* **2014**, *8*, 4940–4947.
- (26) Tang, Q. *J. Mater. Chem. C* **2018**, *6*, 9561–9568.
- (27) Patra, T. K.; Zhang, F.; Schulman, D. S.; Chan, H.; Cherukara, M. J.; Terrones, M.; Das, S.; Narayanan, B.; Sankaranarayanan, S. K. R. *ACS Nano* **2018**, *12*, 8006–8016.
- (28) Gan, X.; Lee, L. Y. S.; Wong, K.; Lo, T. W.; Ho, K. H.; Lei, D. Y.; Zhao, H. *ACS Appl. Energy Mater.* **2018**, *1*, 4754–4765.
- (29) Zhu, J.; Wang, Z.; Yu, H.; Li, N.; Zhang, J.; Meng, J.; Liao, M.; Zhao, J.; Lu, X.; Du, L.; et al. *J. Am. Chem. Soc.* **2017**, *139*, 10216–10219.
- (30) Lin, Y.-C.; Dumcenco, D. O.; Huang, Y.-S.; Suenaga, K. *Nat. Nanotechnol.* **2014**, *9*, 391–396.
- (31) Voiry, D.; Yamaguchi, H.; Li, J.; Silva, R.; Alves, D. C. B.; Fujita, T.; Chen, M.; Asefa, T.; Shenoy, V. B.; Eda, G.; et al. *Nat. Mater.* **2013**, *12*, 850–855.
- (32) Eda, G.; Fujita, T.; Yamaguchi, H.; Voiry, D.; Chen, M.; Chhowalla, M. *ACS Nano* **2012**, *6*, 7311–7317.
- (33) Gaskell, D. R. *Introduction to the Thermodynamics of Materials*; Taylor and Francis: 2008.
- (34) Nam, D.-H.; Kang, H.-Y.; Jo, J.-H. J.; Kim, B. K.; Na, S.; Sim, U.; Ahn, I.-K.; Yi, K.-W.; Nam, K. T.; Joo, Y.-C. *Adv. Mater.* **2017**, *29*, 1605327.
- (35) Nam, D.-H.; Lee, S.; Lee, Y.-J.; Jo, J.-H.; Yoon, E.; Yi, K.-W.; Lee, G.-D.; Joo, Y.-C. *Adv. Mater.* **2017**, *29*, 1702958.
- (36) Beyers, R.; Kim, K. B.; Sinclair, R. J. *Appl. Phys.* **1987**, *61*, 2195.
- (37) Mortazavi, M.; Wang, C.; Deng, J.; Shenoy, V. B.; Medhekar, N. V. *J. Power Sources* **2014**, *268*, 279–286.
- (38) Fang, Y.; Pan, J.; He, J.; Luo, R.; Wang, D.; Che, X.; Bu, K.; Zhao, W.; Liu, P.; Mu, G.; Zhang, H.; Lin, T.; Huang, F.; et al. *Angew. Chem.* **2018**, *130*, 1246–1249.
- (39) Wang, L.; Liu, X.; Luo, J.; Duan, X.; Crittenden, J.; Liu, C.; Zhang, S.; Pei, Y.; Zeng, Y.; Duan, X. *Angew. Chem.* **2017**, *129*, 7718–7722.
- (40) Tang, Q.; Jiang, D. *ACS Catal.* **2016**, *6*, 4953–4961.
- (41) Calandra, M. *Phys. Rev. B: Condens. Matter Mater. Phys.* **2013**, *88*, 245428.
- (42) Linstrom, P. J., Ed. *NIST Standard Reference Database Number 69*; NIST Chem. Webb.: 2003.
- (43) Noh, J.-Y.; Kim, H.; Kim, Y.-S. *Phys. Rev. B: Condens. Matter Mater. Phys.* **2014**, *89*, 205417.
- (44) Lee, J.; Kang, S.; Yim, K.; Kim, K. Y.; Jang, H. W.; Kang, Y.; Han, S. *J. Phys. Chem. Lett.* **2018**, *9*, 2049–2055.
- (45) Pandey, M.; Rasmussen, F. A.; Kuhar, K.; Olsen, T.; Jacobsen, K. W.; Thygesen, K. S. *Nano Lett.* **2016**, *16*, 2234–2239.
- (46) Kim, K. Y.; Lee, J.; Kang, S.; Son, Y.-W.; Jang, H. W.; Kang, Y.; Han, S. *ACS Catal.* **2018**, *8*, 4508–4515.
- (47) Bruix, A.; Lauritsen, J. V.; Hammer, B. 2018, arXiv:1805.01244. arXiv.org e-Print archive. <https://arxiv.org/abs/1805.01244>.
- (48) Kibsgaard, J.; Chen, Z.; Reinecke, B. N.; Jaramillo, T. F. *Nat. Mater.* **2012**, *11*, 963–969.
- (49) Xie, J.; Zhang, H.; Li, S.; Wang, R.; Sun, X.; Zhou, M.; Zhou, J.; Lou, X. W.; Xie, Y. *Adv. Mater.* **2013**, *25*, 5807–5813.
- (50) Yang, L.; Hong, H.; Fu, Q.; Huang, Y.; Zhang, J.; Cui, X.; Fan, Z.; Liu, K.; Xiang, B. *ACS Nano* **2015**, *9*, 6478–6483.
- (51) Shi, J.; Ma, D.; Han, G.-F.; Zhang, Y.; Ji, Q.; Gao, T.; Sun, J.; Song, X.; Li, C.; Zhang, Y.; et al. *ACS Nano* **2014**, *8*, 10196–10204.
- (52) Wang, T.; Liu, L.; Zhu, Z.; Papakonstantinou, P.; Hu, J.; Liu, H.; Li, M. *Energy Environ. Sci.* **2013**, *6*, 625–633.
- (53) Hu, J.; Huang, B.; Zhang, C.; Wang, Z.; An, Y.; Zhou, D.; Lin, H.; Leung, M. K. H.; Yang, S. *Energy Environ. Sci.* **2017**, *10*, 593–603.
- (54) Yan, Y.; Xia, B.; Ge, X.; Liu, Z.; Wang, J.-Y.; Wang, X. *ACS Appl. Mater. Interfaces* **2013**, *5*, 12794–12798.
- (55) Chung, D. Y.; Park, S.-K.; Chung, Y.-H.; Yu, S.-H.; Lim, D.-H.; Jung, N.; Ham, H. C.; Park, H.-Y.; Piao, Y.; Yoo, S. J.; et al. *Nanoscale* **2014**, *6*, 2131–2136.
- (56) Xie, J.; Zhang, J.; Li, S.; Grote, F.; Zhang, X.; Zhang, H.; Wang, R.; Lei, Y.; Pan, B.; Xie, Y. *J. Am. Chem. Soc.* **2013**, *135*, 17881–17888.
- (57) Li, H.; Tsai, C.; Koh, A. L.; Cai, L.; Contryman, A. W.; Fragapane, A. H.; Zhao, J.; Han, H. S.; Manoharan, H. C.; Abild-Pedersen, F.; et al. *Nat. Mater.* **2016**, *15*, 48–53.
- (58) Tao, L.; Duan, X.; Wang, C.; Duan, X.; Wang, S. *Chem. Commun.* **2015**, *51*, 7470–7473.
- (59) Li, G.; Zhang, D.; Qiao, Q.; Yu, Y.; Peterson, D.; Zafar, A.; Kumar, R.; Curtarolo, S.; Hunte, F.; Shannon, S.; et al. *J. Am. Chem. Soc.* **2016**, *138*, 16632–16638.
- (60) Yin, Y.; Han, J.; Zhang, Y.; Zhang, X.; Xu, P.; Yuan, Q.; Samad, L.; Wang, X.; Wang, Y.; Zhang, Z.; et al. *J. Am. Chem. Soc.* **2016**, *138*, 7965–7972.
- (61) Li, Y.; Wang, H.; Xie, L.; Liang, Y.; Hong, G.; Dai, H. *J. Am. Chem. Soc.* **2011**, *133*, 7296–7299.
- (62) Yan, Y.; Ge, X.; Liu, Z.; Wang, J.-Y.; Lee, J.-M.; Wang, X. *Nanoscale* **2013**, *5*, 7768–7771.
- (63) Li, D. J.; Maiti, U. N.; Lim, J.; Choi, D. S.; Lee, W. J.; Oh, Y.; Lee, G. Y.; Kim, S. O. *Nano Lett.* **2014**, *14*, 1228–1233.
- (64) Seo, B.; Jung, G. Y.; Sa, Y. J.; Jeong, H. Y.; Cheon, J. Y.; Lee, J. H.; Kim, H. Y.; Kim, J. C.; Shin, H. S.; Kwak, S. K. *ACS Nano* **2015**, *9*, 3728–3739.
- (65) Chung, D. Y.; Yoo, J. M.; Park, S.; Jung, G. Y.; Kang, J. S.; Ahn, C.-Y.; Kwak, S. K.; Sung, Y.-E. *Small* **2018**, *14*, 1802191.
- (66) Vrabel, H.; Hu, X. *ACS Catal.* **2013**, *3*, 2002–2011.